

# A Novel Distal Hybrid Pneumatic/Cable-Driven Continuum Joint with Variable Stiffness Capacity for Flexible Gastrointestinal Endoscopy

Xiangyu Luo, Dezhi Song, Zhiqiang Zhang, Shuxin Wang,\* and Chaoyang Shi\*

The robot-assisted flexible access surgery represented by the emerging robot-assisted flexible endoscopy (FE) and natural orifice transluminal endoscopic surgery demands flexible and continuum manipulators instead of the rigid and straight instruments in the traditional minimally invasive surgery (MIS). These flexible manipulators are required to advance through the tortuous and narrow anatomic paths via natural orifices for dexterous diagnostic examination and therapeutic operations. Therefore, developing flexible endoscopic manipulators with the capacity of snake-like movements for flexible access and variable stiffness regulation for operations to address these flexible access surgical difficulties is demanding but remains challenging. To address such challenges, herein, it is proposed that a novel distal continuum joint based on the hybrid pneumatic and cable-driven approach achieves variable stiffness capacity, excellent bending characteristics in both flexible and rigid states, satisfactory motion consistency and shape-locking ability during the rigid-flexible transition, and relatively high loading capacity for flexible gastrointestinal endoscopic robots. Characterization experiments validate these performances, and phantom and ex vivo experiments have been performed to demonstrate the feasibility and effectiveness for FE. The presented method demonstrates an effective and practical approach to enabling continuum robots with both flexible access and tunable stiffness capacity and supports a convenient extension for MIS applications.

## 1. Introduction


The emerging robot-assisted flexible endoscopy (FE) and natural orifice transluminal endoscopic surgery (NOTES) transverse through the tortuous and narrow anatomic paths inside human bodies from natural orifices, aiming at dexterous screening and the diagnosis of target diseases and further operational treatment.<sup>[1,2]</sup> These emerging techniques represented the development tendency in flexible access surgery, which demands transcending the techniques in traditional laparoscopic surgery that include both multiport surgery and single-port surgery (SPS).<sup>[3,4]</sup> They are typically designed using flexible and continuum manipulators instead of rigid and straight instruments in the traditional minimally invasive surgery (MIS) to adapt to flexible access.<sup>[5–10]</sup> These developed flexible manipulators are equipped with instrument channels for surgical instruments (e.g., forceps or a variety of electrotomes), empowering surgeons to perform complex and delicate operations.<sup>[11,12]</sup> Therefore, such a complex process requires the performance of flexible endoscopic robots that

can be switched between two working states: the flexible state and the rigid state.<sup>[13–15]</sup> In the flexible state, the distal continuum joint can perform snake-like movements to pass through winding anatomical pathways without damaging tissues. In the rigid state, the distal continuum joint keeps its body shape against external forces and provides sufficient operational forces when surgical instruments interact with target lesions. However, it remains challenging to achieve the highly required capacity of flexible access and continuous variable stiffness regulation to address different surgical scenarios and meanwhile reach an adequate balance between them. As a result, developing continuum joints with variable stiffness techniques for flexible endoscopic robots has become critical and attracted broad attention and investigation.

The design approaches of continuum joints are generally grouped into two main categories of discrete and continuum types. The discrete type typically connects a series of specially designed rigid mechanical joints, such as rolling friction or gear-based joints,<sup>[16–18]</sup> hinged-based joints,<sup>[19]</sup> and revolved sliding joints,<sup>[20,21]</sup> to achieve bending motions in a relatively large

X. Luo, D. Song, S. Wang, C. Shi  
Key Laboratory of Mechanism Theory and Equipment Design of Ministry of Education  
School of Mechanical Engineering  
Tianjin University  
Tianjin 300072, China  
E-mail: shuxinw@tju.edu.cn; chaoyang.shi@tju.edu.cn

Z. Zhang  
School of Electronic and Electrical Engineering  
University of Leeds  
Leeds LS2 9JT, UK

 The ORCID identification number(s) for the author(s) of this article can be found under <https://doi.org/10.1002/aisy.202200403>.

© 2023 The Authors. Advanced Intelligent Systems published by Wiley-VCH GmbH. This is an open access article under the terms of the Creative Commons Attribution License, which permits use, distribution and reproduction in any medium, provided the original work is properly cited.

DOI: 10.1002/aisy.202200403

range by the tendon-driven approach. However, they commonly suffer from nonuniform and inconsecutive bending curvature or shape. The continuum category produces bending motions based on the elastic property of the utilized materials and yields a smooth deflection shape. Typical designs include the concentric tube,<sup>[22,23]</sup> single/multibackbone continuum joints,<sup>[24–26]</sup> notched-style joints,<sup>[27–30]</sup> and helical spring-like joints.<sup>[31]</sup> However, the above-mentioned design schemes rarely show concerns that flexible endoscopic robots are required to perform smooth transitions between flexible and rigid states. Few attempts have focused on the design of continuum joints with continuous stiffness regulation capacity. Therefore, it is necessary to develop and integrate variable stiffness modules into the continuum joints to address the challenges of flexible screening and continuous variable stiffness regulation for different operational scenarios in flexible endoscopy.

The working principles for variable stiffness techniques can generally be dichotomized: the domains of materials and structures. The material-based approaches primarily realize tunable stiffness by changing the intrinsic material properties with external stimulation, including low melting point alloys (LMPA),<sup>[32–34]</sup> the thermoplastic polymer,<sup>[35,36]</sup> shape-memory materials,<sup>[37,38]</sup> rheological fluids (electro- and magneto-rheological fluids),<sup>[39,40]</sup> and so on. Despite the high stiffness-changing ratio values, the phase transition process is time consuming. Their prototypes typically require an energy exchanger, resulting in larger joint diameters, poor biocompatibility, and high leakage risks. The other solution for stiffness adjustment is structure-based technologies, including unit-locking mechanisms,<sup>[41,42]</sup> antagonistic arrangements,<sup>[43–48]</sup> jamming-based methods,<sup>[49–53]</sup> etc. The unit-locking mechanisms commonly adjust the stiffness by reorganizing the mechanical engagement among internal discrete structural units. However, the complex structures pose difficulties for diameter miniaturization. The discrete structural configuration causes discontinuous bending motion and nonuniform curvature, making it difficult to be applied in endoscopic surgery. To reduce the structural sizes, the antagonistic arrangements take advantage of the cable tension to enhance stiffness. However, these arrangements are prone to generate uneven, nonlinear, and dynamic interaction forces among the internal structures. Excessive tension further increases the possibility of structural failure, introducing risks to surgical operations. In addition, jamming-based methods rely on pressure-induced friction to generate geometrical and structural redistribution for continuous stiffness change via the usage of particles, fibers or layers. Negative pressure-based jamming methods are widely utilized for robot-assisted FE to achieve stiffness regulation of flexible joints. However, the typical maximum negative pressure that can be achieved is around 0.1 MPa, which means that the increase in structural stiffness is rather limited.

The continuum joints with variable stiffness capacity for FE still have the following issues to be addressed. Most continuum joints with variable stiffness ability typically cause poor bending performance in the rigid state. This drawback further seriously affects motion control, which is less reported and rarely engaged. The other common issue is that most current designs excessively emphasize the variable stiffness ratio but ignore the stiffness regulation range that needs to fit the operation requirements for endoscopy.<sup>[54]</sup> Furthermore, most current studies focus on

investigating the design methods for general stiffness regulation. However, they have not engaged in the actual requirements for FE, especially for the embedded functional channels for air/water and instruments.

This article presents a novel hybrid pneumatic/cable-driven distal continuum joint with variable stiffness capacity for flexible gastrointestinal (GI) endoscopy. This design combines the principle of jamming with the continuum structure by embedding flat air tubes into the helical continuum structure circumferentially. The structural stiffness of the proposed joint can be continuously adjusted through the interaction friction between the helical structure segment and the air tubes by regulating the positive input pressure. Such design makes it possible to achieve satisfying performance in bending curvature characteristics in both flexible and rigid states. The characteristic experiments have been conducted to investigate performances in bending curvature, rigid-flexible conversion, and loading capacity. Both phantom and ex vivo experiments have been performed to demonstrate the effectiveness of the proposed scheme for FE with regard to the flexibility for access and rigidity for operation.

## 2. Materials and Methods

### 2.1. Design Specifications of the Proposed Distal Continuum Endoscopic Joint

This article aims to develop a continuum joint with variable stiffness capacity for flexible gastrointestinal endoscopy. The design specifications are listed as follows: 1) The bending range of the continuum joint typically achieved more than 90° to support the surgical instruments to perform endoscopic operations.<sup>[55]</sup> 2) According to the existing continuum joint designs, the length of the proposed joint typically ranged from 80 to 120 mm for robot-assisted flexible endoscopic operations.<sup>[55,56]</sup> The distal continuum joints for flexible gastrointestinal endoscopy were typically equipped with 3 or 4 functional channels, including one camera channel, one or two instrument channels, and one water/air channel. The outer diameter of the continuum joint was acceptable in the range from 16 to 22 mm for accessing the gastrointestinal tract, considering that the continuum joint could provide 2 instrument channels for bimanual operation.<sup>[55,57,58]</sup> 3) The loading capacity for human soft tissue operations, such as pulling forces in the GI tract, had been measured as 2.26N for damaged tissues.<sup>[59]</sup> 4) The transition time between the two states shall be as short as possible to achieve an effective transition between flexible access and intraoperative manipulation, as well as quickly responding to emergencies during surgery.<sup>[15]</sup>

### 2.2. Structural Design and Working Principle of the Proposed Distal Continuum Endoscopic Joint

#### 2.2.1. The Detailed Mechanical Design of the Continuum Joint with Variable Stiffness Capacity

The schematic view of the designed robotic distal continuum joint with variable stiffness capacity is illustrated in **Figure 1a**. The proposed flexible joint primarily included a cable-driven

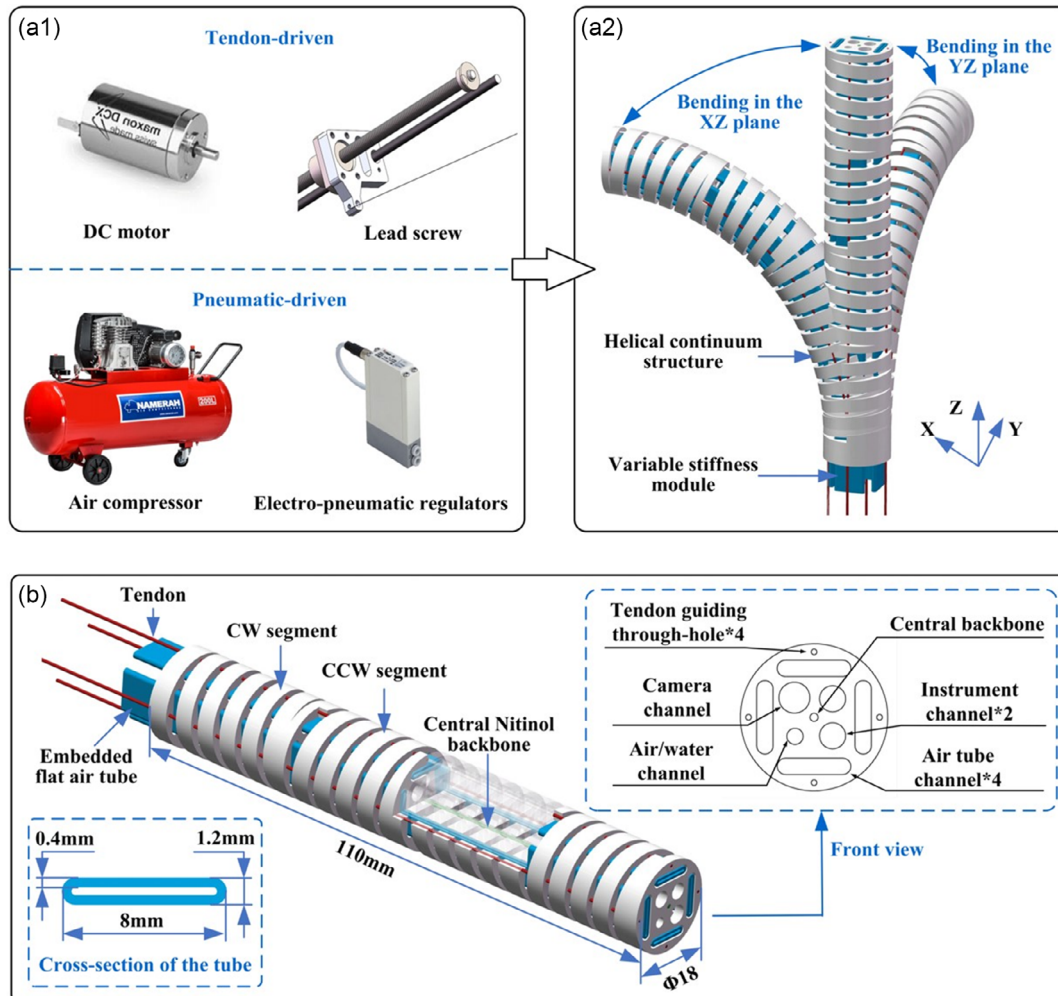


**Figure 1.** The designed structure of the proposed variable-stiffness continuum joint; a1) Driving methods for the continuum joint; a2) The illustration of 2-DOF bending movements; b) The detailed design and cross-sectional configuration of the proposed joint.

helical spring-like continuum structure with a central backbone and an embedded pneumatically driven variable stiffness module. This joint was designed with an outer diameter of 18 mm and an overall length of 110 mm and achieves a 2-DOF bending. As illustrated in Figure 1b, the presented distal helical spring-shaped continuum structure consists of both counterclockwise (CCW) and clockwise (CW) segments configured in pairs. The helical structure exhibited the performance of favorable compliance and high resilience and achieves bending motion with 2 DOFs. The stress was uniformly distributed on the helical structure when bent, and the total structural length to bear the stress distribution was longer than the other types of flexible joints. These features led to reduced stress concentration, outstanding constant bending curvature characteristics, and improved bending repeatability. The configuration of CCW and CW segments in pairs can improve torsion resistance capacity, reduce torsional deformation, and minimize force-induced elongation. A super-elastic nitinol rod (OD = 0.8 mm) was assembled inside the central channel of this helical structure with its two ends glued and fixed to serve as a backbone. This backbone assembly enhanced

axial and radial stiffness, prevented unexpected axial compression, and produced excellent bending resilience due to its super-elasticity. The embedded pneumatically driven variable stiffness module was actuated with four flat air tubes arranged by an equal interval of 90° inside the circumference of the helical structure. The evenly distributed friction force between the inflatable air tubes and the helical structure increased the stiffness of the designed flexible joint and improved its loading capacity. The cross-sectional profile of the utilized flat air tube was rectangular shaped with rounded corners (8 mm width, 1.2 mm height, and 0.4 mm thickness) instead of the traditional circular shape, as displayed in the bottom left of Figure 1b. This profile provided more contact area between the air tube and the helical structure to generate sufficient interaction force. Meanwhile, such a tube shape induced more significant radial deformation than its axial deformation when inflated. This function generated a negligible effect on the bending shape of the designed continuum joint and thus produced satisfactory motion consistency and shape-locking ability during the flexible–rigid transition process. Furthermore, the air tubes achieved high-pressure values to enhance structural

stiffness with a small volume of compressed air, which demonstrated intrinsic safety for practical surgery.

The cross-sectional layout of the presented continuum joint had been configured for FE, as illustrated in the top right of Figure 1b. It was equipped with one 3.8 mm diameter camera channel, two instrument channels with the same diameter of 3.2 mm, one 2 mm water/air channel, and four circumferential through holes to pass the driving tendons. The imaging and instrument channels were designed to carry an endoscope and surgical instruments for examination and functional operations. The pulling tendons pass through the guiding holes made along the continuum joint, and their distal ends were assembled at the end of the helical structure with knots to control the bending movements. The layout of these available channels was learned from the configuration of the commercial endoscopy, which provided sufficient space for the endoscope and surgical instruments. The detailed dimensional parameters are presented in Table 1.

**Table 1.** The dimensions of major components.

Component	Dimension [mm]
The total length	110
Overall outer diameter	18
Backbone diameter	0.8
Tendon guiding through holes diameter	0.7
Tendon diameter	0.5
Instrument channel diameter	3.2
Endoscopic channel diameter	3.8
The air/water tube channel diameter	2

### 2.2.2. Working Principle of the Stiffness Regulation Approach

The proposed continuum joint provided variable stiffness regulation capacity and works in both flexible and rigid states. The working principle is illustrated in Figure 2a. The friction between the flat air tubes and the inner wall of the helical structure was mainly determined by the contact area and contact pressure between them. The contact area gradually increased with the expansion of the air tubes until the air tubes were fully in contact with the helical structure. The contact pressure can be tuned by controlling the input pressure of the air tubes.

When the air tubes were not inflated or inflated with slight pressure, the continuum joint worked in its flexible state, as shown in Figure 2b. Under this state, the helical spring-like continuum structure and the Nitinol backbone played the dominant roles. They can perform satisfactorily regarding excellent constant bending curvature characteristics and moderate structural stiffness. The continuum joint shifted to its rigid state when the air tubes were inflated with sufficient pressure, as displayed in Figure 2c. As the pressure increased, the distributed friction between the inside wall of the helical structure and the air tubes greatly enhanced, preventing the relative movement among each other and increasing the structural stiffness. Meanwhile, the homogeneous interaction between the helical structure and the flat tubes led to the uniform distribution of the internal friction force. This merit benefits this flexible joint with excellent constant curvature characteristics in the rigid state. The pneumatically driven approach and the distributed contact area supported the internal friction adjustment by digital control of the input air pressure, leading to the continuous variable stiffness regulation. Thus, the continuum joint was empowered to control structural rigidity and improve its loading capacity. Furthermore,

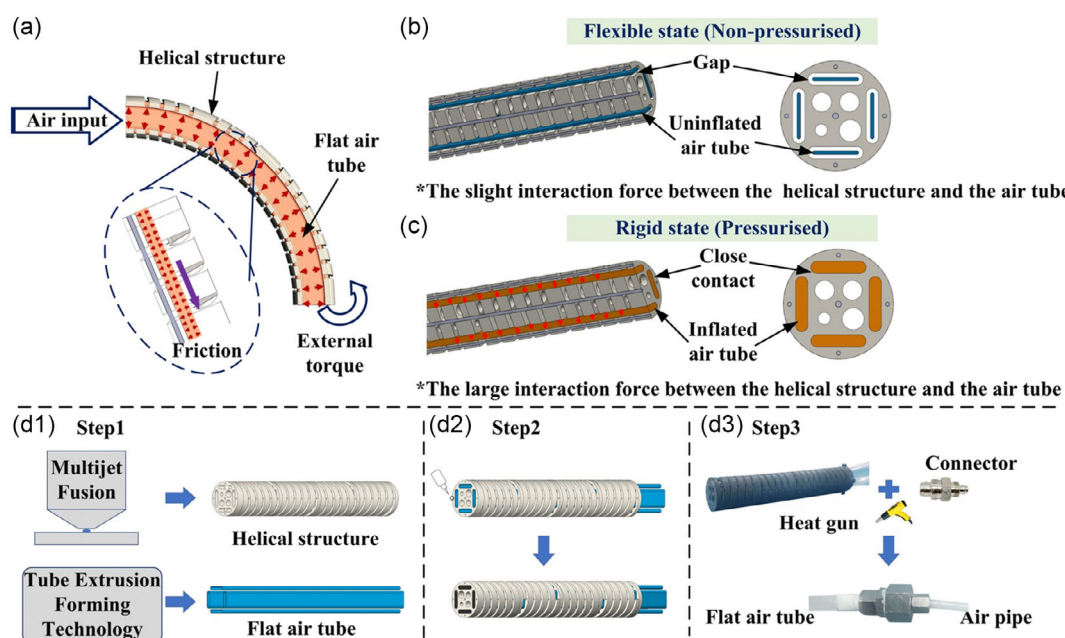


**Figure 2.** The working principle and implementation of the proposed stiffness regulation method: a) Working principle illustration of the stiffness adjustment; b) Deflating/uninflated conditions in the flexible state; c) Inflating condition in the rigid state; d) The assembly process of the flat air tubes and the helical structure.

the conversion between the flexible and rigid states was completed rapidly due to the air tube-based pneumatically driven approach, making it an excellent candidate for emergency response in clinical scenarios.

### 2.3. Fabrication and Assembly of the Distal Continuum Joint

The detailed fabrication and assembly between the continuum structure and the pneumatically driven modular consist of three steps, as illustrated in Figure 2d. First, the designed helical structure was manufactured by HP's exclusive MJF (Multijet Fusion) 3D printing method using nylon (HP3DHR-PA12), as shown in Figure 2d1. The utilized nylon material possesses high strength and toughness attributes, making it especially suitable for producing large deformation without damage. The flat air tube was formed by tube extrusion forming technology with thermoplastic polyurethane (TPU). This material was used because of its softness in the noninflatable state. It can quickly expand and deform to realize the stiffness regulation and generate negligible effects on the continuum joint's bending deformation in the flexible state. Second, the four flat air tubes passed through the channels made inside the helical structure and then were fixed at their distal ends using acrylate adhesive for assembly, as shown in Figure 2d2. To achieve sufficient bonding strength, a two-step bonding method with two different types of glue has been utilized to achieve stable bonding. The detailed bonding process can be divided into the following two steps: 1) the cyanoacrylate adhesive (CA40H, 3M, US) was applied to effectively fill the gap between the NiTi rod and central backbone channel due to its great liquidity and 2) the acrylate adhesive (K9119TM, Kafuter, CN) was pasted around the intersection of the NiTi rod and the end cross-section of the helical structure to further improve the bonding effect due to its high bonding strength. The joint was kept quiescent for 12–24 h to solidify the glue after each glue usage. Third, the proximal ends of the four flat air tubes were pneumatically driven, as shown in Figure 2d3. A heat gun was utilized to heat and soften the proximal end of the flat air tubes to improve connection sealing quality.

### 2.4. Hardware Configuration of the Control and Driving Units

The experimental hardware configuration had been designed, as illustrated in Figure 3. It mainly includes a tendon-driven part for motion control, a pneumatic-driven part for stiffness adjustment, and an imaging camera. The tendon-driven part comprises a PMAC motion controller, 5 PNEP drivers, and 5 linear actuation units. The PMAC serves as the motion controller to communicate with the host PC and control 5 motors with an EtherCAT connection. The tendon-driven part includes 4 linear modules to realize the 2-DOF bending motion and 1 linear module to achieve the translation movement for the proposed distal flexible joint. Each of these linear modules comprises a DC motor (DC-max 16S), a motor driver (PNEP-2/48-Y-S), and a ball screw guide rail. The pneumatic-driven part consisted of an air compressor, two electro-pneumatic (E/P) regulators (ITV0030-3BL, SMC, JPN), and two solenoid valves (VT307-5G1-01, SMC, JPN) controlled by an EtherCAT I/O module. The input air generated by the air compressor (1600W-30L, OTS, CN) was divided into two routes through a three-way valve (KQ2T04-00A, SMC, JPN). The input pressure of the E/P regulator was adjusted and the real-time pressure for control was calculated. One of the two routes was connected with a pair of flat air tubes arranged symmetrically and the stiffness of the proposed joint was adjusted. The E/P regulator and the solenoid valve were controlled by an EtherCAT I/O module for pressure regulation in each route. The I/O module was connected to the PC to get the control command and send the feedback data at 1000 Hz. The digital camera with a resolution of  $1920 \times 1080$  (C930C, Logitech, CN) measured the distal position of the designed joint. Besides, a coordinate frame was established at the proximal end of the flexible joint to describe the motion plane.

## 3. Experiments and Results

### 3.1. Curvature Characterization of the Proposed Continuum Joint in the Flexible and Rigid States

The proposed continuum joint was driven to bend in the range of  $[-90^\circ, 90^\circ]$  with an interval of  $10^\circ$  to experimentally investigate its

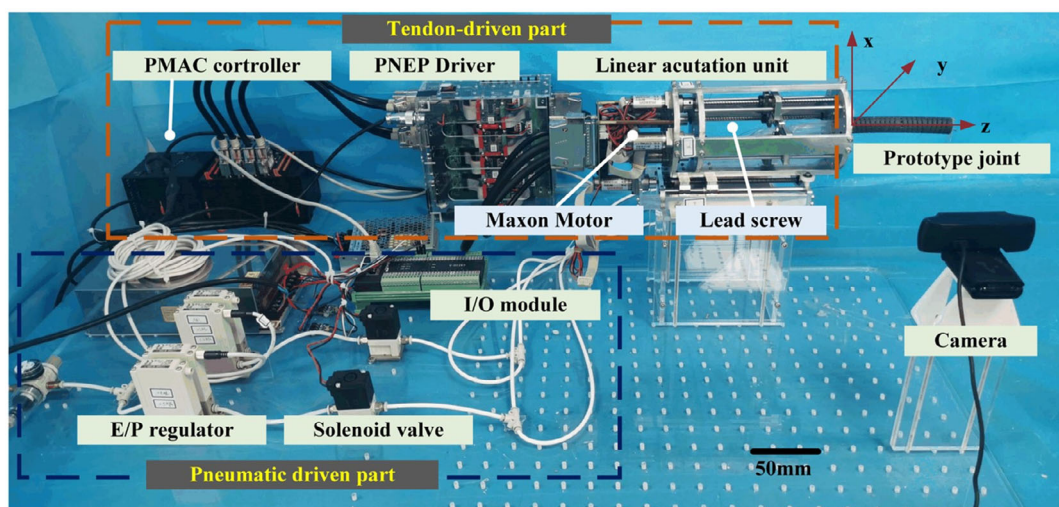


**Figure 3.** Hardware configuration of the control and driving units.

bending curvature characteristics in the flexible and rigid states with the input pressure of 0 and 500 kPa, respectively, as illustrated in Figure 4a1,b1, c1, d1. This experimental process was performed three times, and the corresponding trajectories of the distal end have been dotted in the middle part of Figure 4. The theoretical kinematic results based on the constant curvature modeling assumption from configuration space to task space have been illustrated with a green curve in the XZ plane and a blue curve in the YZ plane for the flexible state in Figure 4a2,c2 and for the rigid state in Figure 4b2,d2. The minimum, average, and maximum error values were calculated to evaluate the distal deflection under the two states, as listed in Table 2 and 3. The relative ratios of the average error accounting for the total length of the flexible joint (110 mm) were 2.19% (2.41 mm) in the XZ plane and 1.98% (2.18 mm) in the YZ plane for the flexible state. These values were 2.35% (2.59 mm) and 2.55% (2.80 mm) for the rigid state. These results indicate that the 2-DOF joint possesses excellent constant bending curvature characteristics in both flexible and rigid states. Meanwhile, the

**Table 2.** The distal positioning error of the proposed joint in the flexible state.

Distal position error	XZ plane <sup>a)</sup>	YZ plane <sup>a)</sup>
Minimum error	0.48 mm (0.44%)	0.58 mm (0.53%)
Average error	2.41 mm (2.19%)	2.18 mm (1.98%)
Maximum error	6.59 mm (5.99%)	5.31 mm (4.83%)

<sup>a)</sup>Percentage data in parentheses represent relative errors accounting for the total length of the flexible joint (110 mm).

proposed joint can change its bending shape continuously in the rigid state, which is rarely mentioned or developed in the current literature. It demonstrates an ideal capacity and is a candidate for endoscopic operations to realize accurate movements with suitable stiffness.

The hysteresis tests have also been performed in the XZ and YZ planes to explore the influences of the friction-based variable

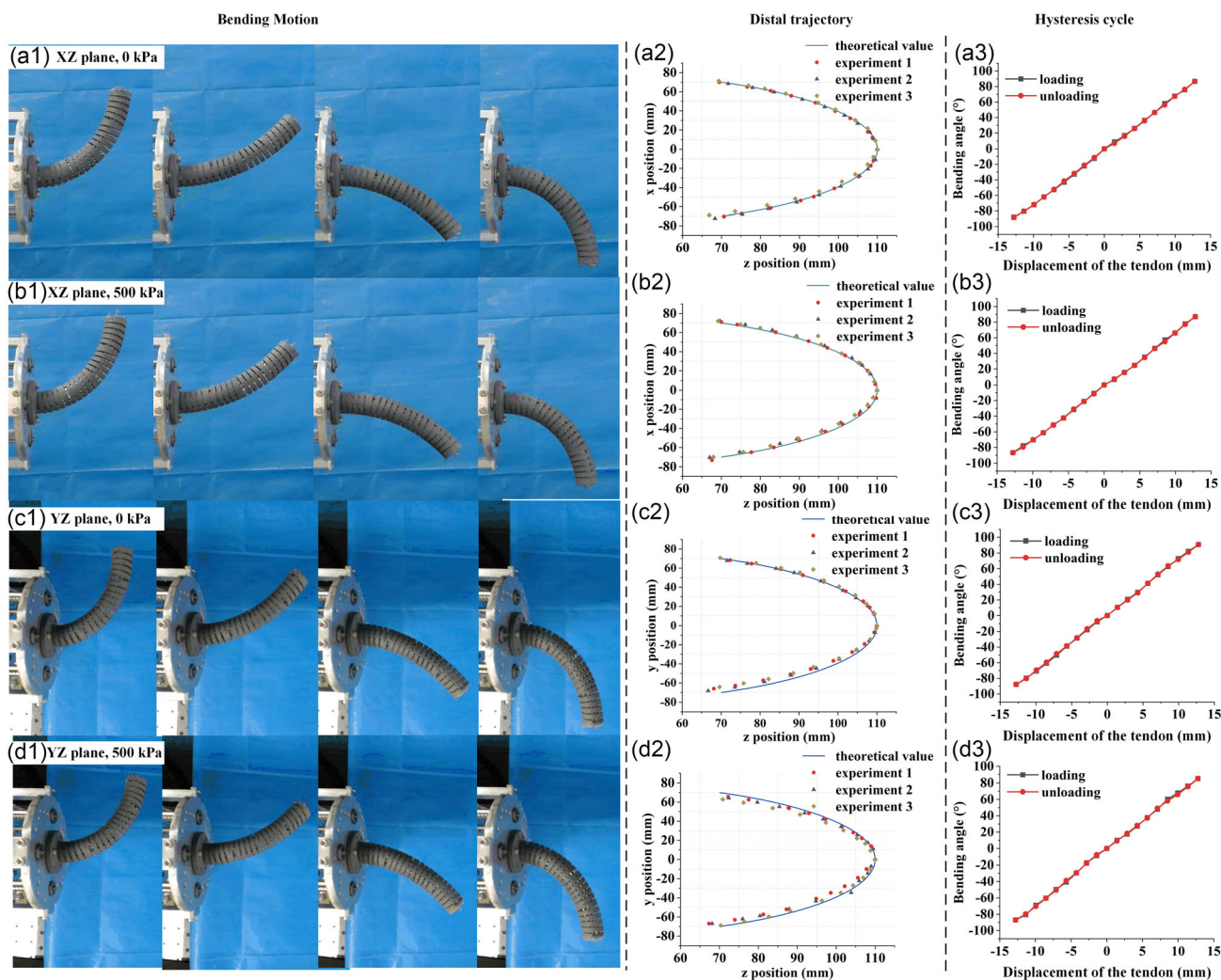


**Figure 4.** Experiments of curvature and hysteresis characterization for the proposed continuum joint: a) The flexible state in the XZ plane; b) The rigid state in the XZ plane; c) The flexible state in the YZ plane; d) The rigid state in the YZ plane.

**Table 3.** The distal positioning error of the proposed joint in the rigid state.

Distal position error	XZ plane <sup>a)</sup>	YZ plane <sup>a)</sup>
Minimum error	0.49 mm (0.45%)	0.64 mm (0.58%)
Average error	2.59 mm (2.35%)	2.80 mm (2.55%)
Maximum error	6.88 mm (6.25%)	5.64 mm (5.13%)

<sup>a)</sup>Percentage data in parentheses represent relative errors accounting for the total length of the flexible joint (110 mm).

stiffness mechanism. The relationships between the displacement of the driving tendon and the bending angle in the flexible and rigid states are shown in the right part of Figure 4. In the flexible state, the average hysteresis errors were 1.99% in the XZ plane and 1.92% in the YZ plane. These values were 2.34% and 2.13% for the rigid state. These results reveal that the proposed continuum joint demonstrates excellent motion consistency in the loading and unloading phases for both flexible and rigid states with negligible hysteresis errors.

### 3.2. The Shape-Locking Performance During the Flexible–Rigid Transition

The stiffness regulation methods for the continuum joint design commonly experience difficulties that include the large distal end deflection variation due to the stiffness change and degraded constant curvature performances during the flexible–rigid transition. The distal deflection difference value between the flexible and rigid states (DDFR) has been defined to quantify the shape-locking performance during the stiffness transition. The smaller DDFR value reflects the smoother flexible–rigid transition process with a slight shape change. The prototype was deflected by 90° with an interval step of 10° in the XZ plane. At each bending angle, the continuum distal deflections of the joint were

measured before and after pneumatic inflation, respectively, as presented in Figure 5a. This deflating and inflating process was repeated three times. In addition, the transition time between the two states at each angle is less than 3 s. The average distal position values at each bending angle for both flexible and rigid states have been illustrated in Figure 5b. The average DDFR value was calculated to be 0.79 mm, accounting for 0.72% of the total length. Such a small shape change value validates that the proposed stiffness regulation method produces a smooth transition and a satisfactory shape-locking capability, which can effectively avoid the abrupt distal change during the flexible–rigid transition. Thus, the proposed method can further support operational accuracy improvement and safety enhancement in practical scenarios with short response time.

### 3.3. Investigation of the Relationship between Structural Stiffness and Air Pressure

To analyze the relationship between the input air pressure inside the flat tube and the structural stiffness of the proposed joint, the typical three-point bending flexural test<sup>[35,52]</sup> was conducted with the experimental setup, as shown in Figure 6a. The suspension span length was 80 mm for all the tests. The driving motor was controlled to move down at a 4 mm min<sup>-1</sup> speed until reaching a central deflection of 2 mm. The force sensor connected to the loading arm recorded the force in real time. The air pressure in the flat air tube started from 0 kPa and gradually increased to 500 kPa with an interval of 50 kPa. Three experiments were performed for each loading air pressure set, and the corresponding average structural stiffness value was obtained. The structural bending stiffness can be estimated using the formula below

$$EI = FL^3\delta^{-1}/48 \quad (1)$$

where EI denotes the production of the flexural rigidity, *F* is the loading force, *L* stands for the support span distance, and  $\delta$  is the deflection displacement.

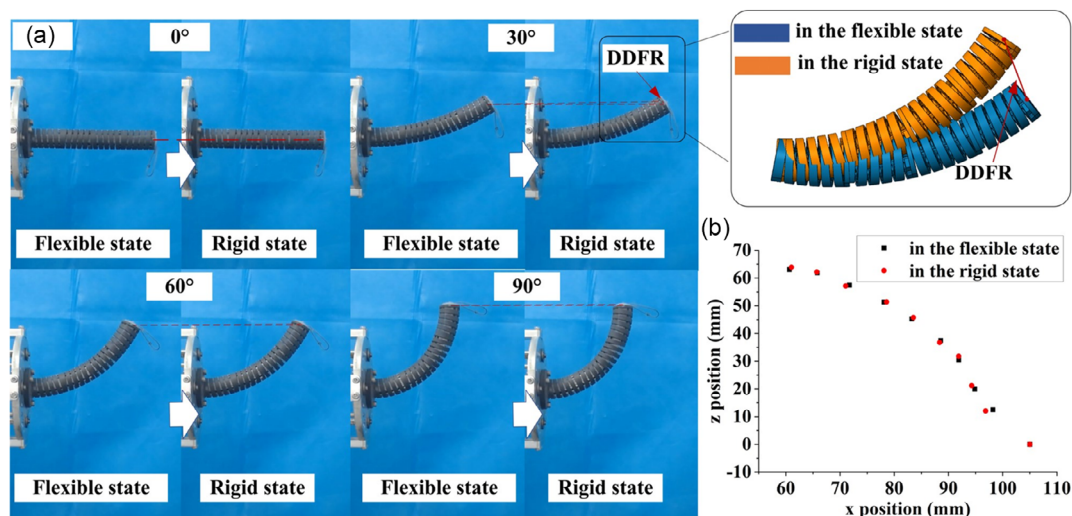


**Figure 5.** Experiments of the shape locking performance during the flexible-rigid transition: a) The bending shape before and after pneumatic inflation; b) The distal positions of the proposed continuum joint at different bending angles in the two states.

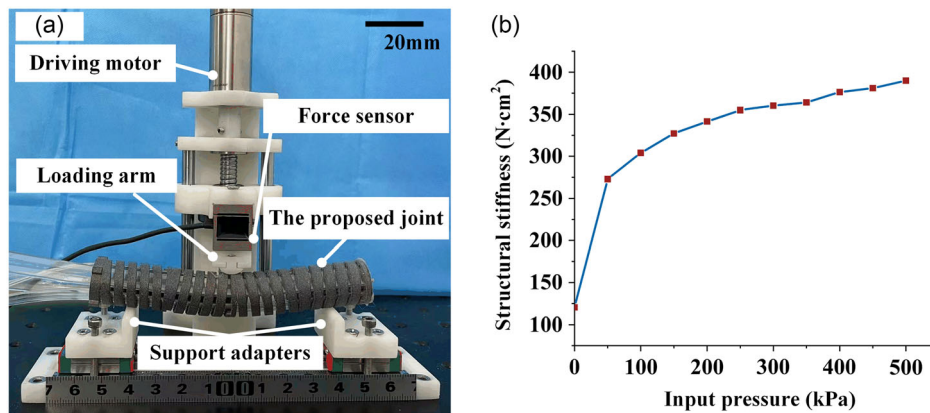


**Figure 6.** Experiments of the relationship between the structural stiffness and the input air pressure: a) The experimental setup of the three-point bending flexural test; b) The experimental results.

The relationship between the input pressure and the structural stiffness showed that the stiffness values were determined as 389.93 and 120.32 N cm<sup>2</sup> for the rigid and flexible states, respectively, as illustrated in Figure 6b. The increase of structural stiffness with the input air pressure can be divided into two stages. When the input air pressure is less than 50 kPa, the structural stiffness increases rapidly with the air pressure, which indicates that the contact area is positively correlated with the input air pressure. When the input air pressure is greater than 100 kPa, the structural stiffness increases with the air pressure increases slowly, which indicates that the air tube is in full contact with the helical structure. Such results verify that the proposed stiffness adjustment method can realize tunable and continuous stiffness with increased air pressure. This merit can further support stiffness control to address the operational demands with different payloads and avoid sudden changes in stiffness and shape.

### 3.4. Experiments for Quantification of Loading Capacity

The distal deflection shapes were recorded when the continuum joint was configured with 0°, 30°, 60°, and 90°, respectively, as illustrated in Figure 7a1,a2. The standard weights were suspended at the distal end to perform the loading experiments with an interval of 10 g in both flexible (0 kPa) and rigid (500 kPa) states. For surgical robots in a master-slave configuration, the deflection of less than 10% of the total length of the continuum joint can be corrected with endoscopic imaging. Therefore, the loading force to generate a distal deflection of 11 mm was utilized to evaluate the loading capacity of the designed flexible joint. These experiments were repeated three times, and the average values of rated loading capacity for the flexible and rigid states are 1.50 and 4.80 N, respectively. The corresponding average values in different bending angles are summarized in Figure 7b. The variable stiffness joint in the rigid state possessed a loading capacity of 3.2 times higher than that of the flexible state. Furthermore, the distal deflection of 11.87 mm was detected with a distal 5 N payload, which meets the general loading requirement.<sup>[60]</sup> These results prove that the proposed variable stiffness approach can effectively improve the loading capacity without sacrificing flexibility.

The limits for loading capacity in the rigid state have been investigated, as shown in Figure 7c. When the input air pressure was 500 kPa, the distal end deflection reached 41.14 mm with a distal weight of 1 kg and maintained the basic shape without causing structural collapse when configured at 90°. In this case, the distal end deflection has been more than 10% of the total length of the continuum structure. It proves that the proposed structure can respond well to extreme loading situations (e.g., cutting conjoined tissues and lifting large and heavy tissues or organs). The loading capacity limits can be further improved with the increased pressure. The distal end deflection decreased to 35.02 mm with the distal weight of 1 kg when the input pressure reached the upper limitation of 800 kPa for the air tube.

### 3.5. Phantom Experiments

To evaluate the dexterity of the proposed design, the experiment on the colonoscopy phantom (Kang Beidian, CN) was performed in Figure 8a. A multilumen tube served as the middle insertion tube, and the distal continuum joint was assembled with it to make the endoscopic manipulator. The 3.6 mm diameter endoscopic camera (WS-MM1-L04, WiserScope, CN, 720p) was assembled to collect intraluminal imaging through the camera channel. Two 2.6 mm diameter endoscopic forceps (Micro-Tech, CN) were arranged through the instrument channels for biopsy operation, as shown in Figure 8b. This 3-DOF manipulator was implemented to actuate the distal continuum joint with the linear modules. The look-and-move scheme was utilized, and the endoscopic manipulator was driven to approach the target lesions in descending colon with considerable flexibility, as illustrated in Figure 8c. This experiment qualitatively proves that the proposed continuum joint could be utilized as a distal flexible overtube assembled in the endoscope for steering insertion and orientation adjustment with considerable flexibility for endoscopic access.

### 3.6. Ex vivo Experiments

The ex vivo experiment has also been performed with the typical organ-pulling operation, as shown in Figure 9a. A TPU tube with



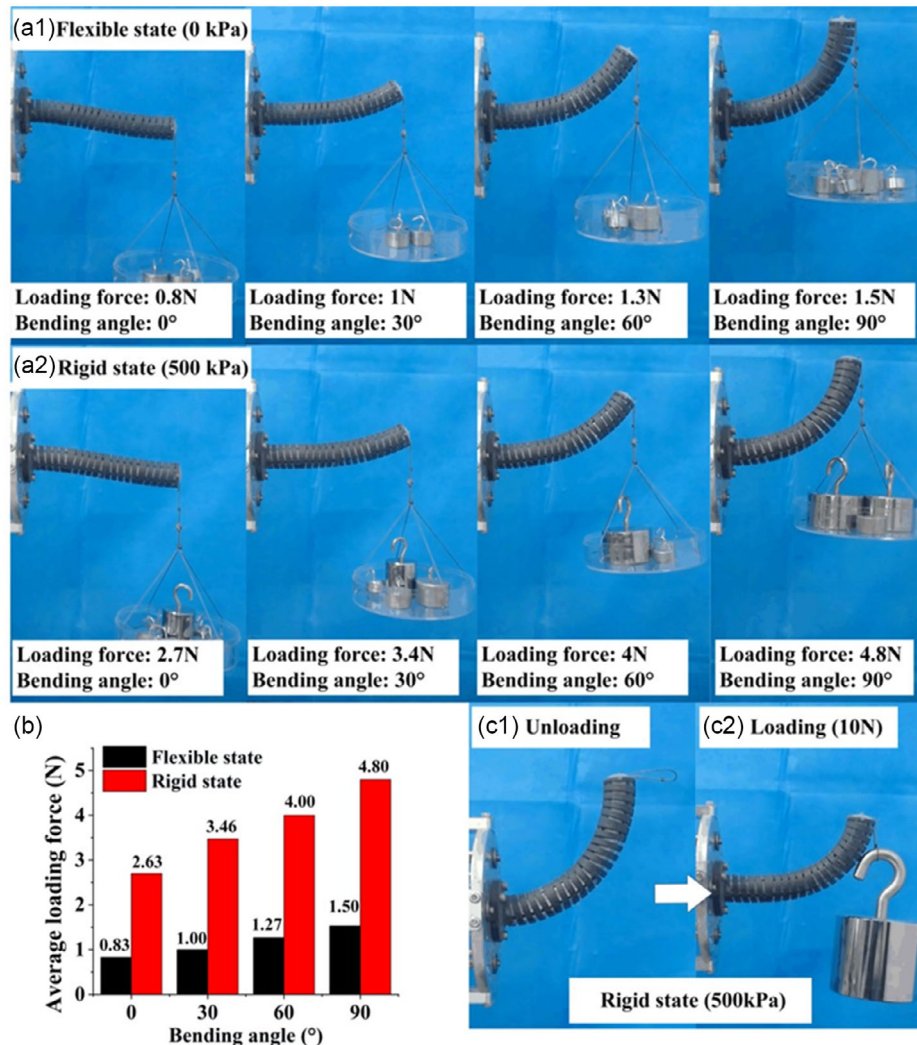


**Figure 7.** Experiments for quantification of loading capacity: a) Loading tests of the proposed joint: a1) The case in the flexible state; a2) The case in the rigid state; b) Average results of the loading tests; c) The investigation on limits of loading capacity; c1) The bending shape in the unloading condition, c2) The bending shape in the loading condition of 10 N.

a diameter of 25 mm was employed to simulate the constraints of the esophagus, and its two ends were fixed on the brackets. The look-and-move scheme was utilized in this experiment. The manipulator was driven to advance inside this TPU tube, and the distal continuum joint was deflected to the same initial shape (90°) and localized to the target site of a pork liver (310 g). The two carried forceps can be moved to the operation area for tissue grasping, as presented in Figure 9c. Then the manipulator was driven back with a displacement of 40 mm in the flexible state and rigid state, respectively. Such operations were repeated three times. The change of the central line of the distal joint, as labeled in Figure 9b, was calculated to reflect the shape change under different states. The three central lines for the initial and final shapes in the flexible and rigid states are illustrated in Figure 9d. Compared with the initial shape before pulling, the distal end position deviation values for the final shapes after pulling at the rigid and flexible states were 4.61 mm and 15.48 mm, respectively, compared with the initial shape. They account for

4.26% and 14.33% of the total length of the flexible joint. By regulating the stiffness of the proposed joint, the distal end position deviation value was reduced by 70.22%, validating the improved loading capacity under the rigid state and the effectiveness of the flexible–rigid transition. Such experimental results indicate that the proposed joint has improved loading capacity to support the performance of complex surgical procedures in the rigid state. Furthermore, compared with other variable stiffness methods, the proposed variable stiffness joint contributes to a potential scheme for flexible endoscope design because it is configured with sufficient functional channels for endoscopic manipulation.

#### 4. Discussion

The comparison with other continuum joints for minimally invasive surgery (MIS) with tunable stiffness has been summarized in Table 4. The proposed design achieves great constant

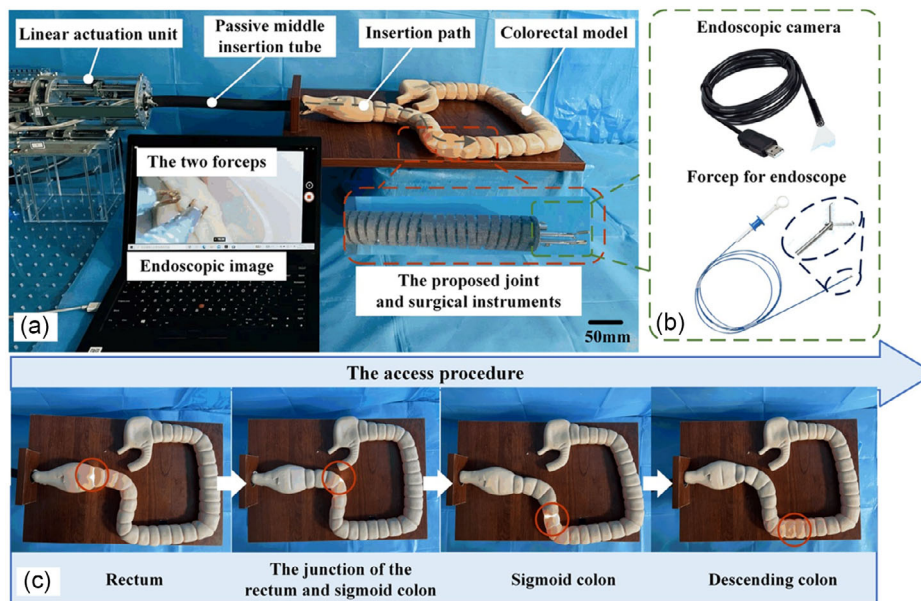


**Figure 8.** The phantom experiments for validation on the dexterity for access using the proposed joint: a) The experimental setup for phantom experiments; b) The utilized endoscopic camera and the forceps in this experiment; c) Illustration of the insertion access process of the designed continuum joint (The red circle represents the actual position).

curvature bending abilities with relative position error values of 2.19% and 2.55% for both the flexible and rigid states. The curvature characteristics in the rigid state are rarely mentioned in the current literature because most designs have difficulty bending motion in the rigid state. The advantages of curvature bending characteristics in both states are due to the following two reasons. On the one hand, the utilized helical structure has high flexibility and uniform structural stress distribution during bending, leading to decreased stress concentration, excellent bending constant curvature performance, and bending repeatability. On the other hand, the interaction between the embedded variable stiffness module and the helical structure is distributed uniformly. Moreover, the influence of the variable stiffness scheme on the motion consistency during loading–unloading phases is rarely mentioned, as shown in Table 4. The hysteresis error values are measured as 1.99% and 2.34% for both flexible and rigid states in the proposed design, reflecting that the proposed stiffness adjustment design based on friction has little effect on motion consistency. These merits support precise motion control and high security for clinic operation.

The material-based variable stiffness schemes generally have a larger flexible–rigid transition ratio and loading force, as shown in Table 4. For instance, Zhao et al. proposed a variable stiffness over tube based on LMPA, which achieved a large payload ratio of 106 between two states and a rated payload of 10 N.<sup>[32]</sup> However, such methods commonly require about 20 s and more for the transition process between the two states, which may bring potential risks to endoscopic procedures. The stiffness regulation process realized by the pneumatic-driven module in this work can be completed within 3 s, which is faster than the other designs in Table 4. This advantage demonstrates the ability of the designed flexible joint to respond quickly, short enough to respond to emergencies during surgery. Meanwhile, the rated

loading of 1.5 N for the flexible state and 4.8 N for the rigid state is provided in the presented design, which was sufficient for most operations in endoscopic surgery.

The comparison among the existing continuum joints with variable stiffness for the overall outer diameter and the number of functional channels has also been summarized in Table 4. The proposed design with variable stiffness capacity further exhibits excellent integration performance with two instrument channels for surgical instruments and is configured with an outer diameter of 18 mm. Such configuration enables the simultaneous manipulation of two surgical instruments for endoscopic tissue operations. The feasibility of the proposed joint has been verified in the phantom and ex vivo experiments regarding flexibility for access and rigidity for operation. The diameter values of commercial gastrointestinal endoscopes for digestive tracts are typically 9–15 mm,<sup>[61]</sup> while the diameter of the existing flexible endoscope robots varies within a range of 16 to 22 mm for gastrointestinal applications.<sup>[57,58]</sup> Commercial gastrointestinal endoscopes are commonly equipped with a light guide lens, a water jet, an objective lens, an air/water nozzle, and one instrument channel. This diameter will undoubtedly increase if the endoscopes are required to either carry two instruments or add the stiffness adjustment function. For instance, the robotic endoscope diameter in research<sup>[58]</sup> reaches 17 mm with two instruments but lacks the stiffness adjustment function; the endoscope design in research<sup>[32]</sup> reaches 17 mm in diameter with the stiffness adjustment function but provides only one central hollow channel. Therefore, the designed outer diameter is reasonable compared with other flexible gastrointestinal endoscope robots. The proposed method presents an effective and practical design to be integrated into the distal end of gastrointestinal endoscopes with the additional functions of stiffness adjustment and support dual-instrument manipulation. The proposed

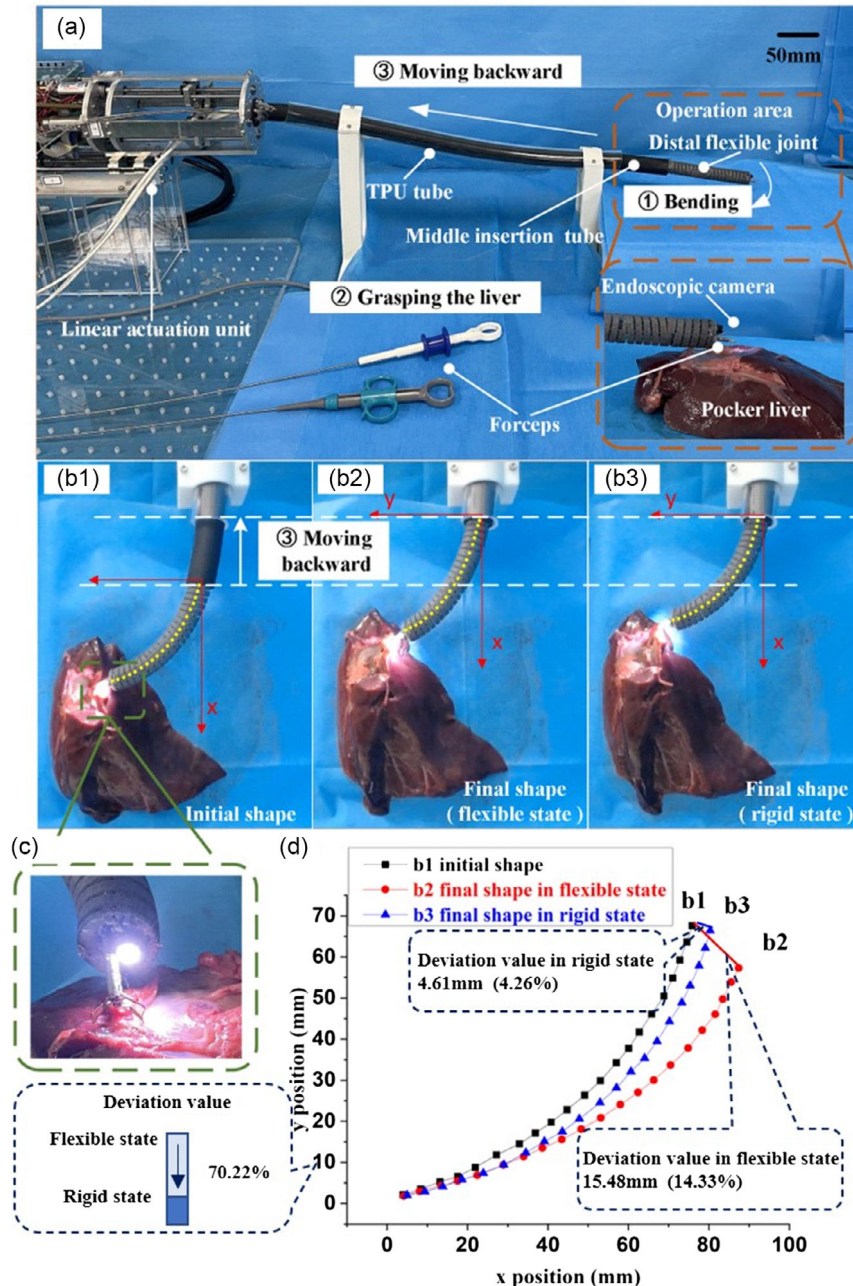


**Figure 9.** The ex-vivo experiments for organ-pulling operations using the proposed joint: a) The ex-vivo experimental setup; b) Shape comparison of the continuum joint at different states: b1) The initial shape; b2) The final shape in the flexible state; b3) The final shape in the rigid state; c) Illustration of the distal interaction; d) Comparison of the experimental results for these shapes.

flexible joint can further decrease its diameter to 13 mm by customizing air tubes of smaller sizes and adapting metal 3D printing technology with higher precision. If the instrument number can be reduced, the diameter can be further downsized. However, the purpose of gastrointestinal endoscopes needs to support both diagnostic examinations and therapeutic operations. The integration of instrument channels supports operations for complex diseases. The assistant channel of the air/water nozzle is quite helpful in clearing the internal effusion and bubble to clear the field of view before effective examination

and operation. Such functional channels are indispensable and cannot be removed. These requirements make it difficult to further downsize the overall diameter for the GI endoscopes.

If targeting other fields, such as interventional robotic devices, the proposed method can be applied but need further improvements. For the interventional robotic devices at several millimeters,<sup>[62–64]</sup> the friction is still closely related to the positive pressure and friction coefficient between the two bodies in contact. The proposed method can be directly applied to the distal continuum joint of the interventional devices for stiffness

**Table 4.** The performance comparison of the continuum joints with variable stiffness capacity.

Approach	Stiffness adjustment principle	Relative position error <sup>a)</sup>	Bending range	Relative hysteresis error <sup>a)</sup>	Payload ratio between the two states	Rated loading capacity (deflection)	The transition time between the two states <sup>a)</sup>	Overall outer diameter	Number of FC (IC) <sup>b)</sup>	The inner diameter of FC	Medical application <sup>c)</sup>
Material-based methods	LMPA <sup>[32]</sup>	\	\	\	Approximately 106	10N (2%)	17s(R→F) 18s(F→R)	17 mm	1 (1)	φ10 mm	FE
	Thermoplastic PET <sup>[35]</sup>	\	\	\	22	3.5N (12.8%)	12s(F→R) 15s(R→F)	15 mm	2 (2)	φ3.5 mm	FE
	Thermoplastic starch <sup>[36]</sup>	\	\	\	92.3	4N (10%)	165s(F→R) 28s(R→F)	15.5 mm	0	\	MIS
	SMA <sup>[37]</sup>	\	\	\	1.4	1.45N (16.7%)	18s(F→R) 60s(R→F)	13 mm	0	\	SPS
Structure-based methods	Units locking <sup>[41]</sup>	\	\	\	3.2	0.6N (47.5%)	\	13 mm	1 (\)	\	FE
	Cable tension <sup>[43]</sup>	\	±180°	7.87% (R)	Approximately 2.5	2.5N (7.7%)	\	15.9 mm	1 (1)	φ9.86 mm	FE
	Tube insertion <sup>[44]</sup>	2.72%(F)	±180°	\	10.83	\	2s(R→F) 3s(F→R)	7.4 mm	0	\	SPS
	Granular jamming <sup>[49]</sup>	3.75%(F)	±90°	\	1.46	5.95N (10%)	\	32 mm	0	\	SPS
	Fiber jamming <sup>[50]</sup>	2.3%(F)	171°	\	1.6	0.9N (20%)	\	14.5 mm	1 (1)	φ4.5 mm	SPS
	Layer jamming <sup>[51]</sup>	\	\	\	Approximately 1.9	4N (5%)	\	24 mm	1 (1)	φ15mm	MIS
	Cable jamming <sup>[53]</sup>	\	\	\	Approximately 2	\	\	5.5 mm	0	\	FE
The proposed design	2.19% (F) 2.55% (R)	±90°	1.99% (F) 2.34% (R)	3.2	4.8N (10%) 10N (36.3%)	Both less than 3 s	18 mm	4 (2)	1 × φ3.8 mm; 1 × φ 2 mm; 2 × φ3.2 mm	FE	

<sup>a)</sup>R: the rigid state; F: the flexible state. <sup>b)</sup>FC: functional channels; IC: instrument channels. <sup>c)</sup>FE: flexible endoscopy; SPS: single-port surgery; MIS: minimally invasive surgery.

adjustment with the reduced pipeline size. This pneumatic/air-operated driven approach can also be replaced by the hydraulic-driven method for vasculature interventions. The hydraulic-driven method has already been implemented by the Ikuda group at Nagoya University to make active multi-segment catheters with outside diameters of 3 mm.<sup>[64,65]</sup> The hybrid micro stereolithography process was utilized for fabrication, and tiny valves were made to provide different pressure threshold values to facilitate the bending motions of different segments of catheters.<sup>[64,65]</sup> For the interventional robotic devices at the micron level,<sup>[66]</sup> the typical MEMS technology can support the easy fabrication of microfluidic channels to support both air and liquid flow, and the micro stereolithography technique can empower the design of multiple segments to support stiffness tuning.<sup>[65]</sup> Given the scaling laws, the surface-relevant force, e.g., friction will be more dominant than the volume-relevant force, e.g., gravity. The lengthy microfluidic channels can be made using MEMS techniques to further increase the contact surface. Thus, the impactful friction may cause more drastic stiffness changes since the presented stiffness modulation depends on friction.

The closed-loop control for robotic endoscopic systems is also essential for precise operations. Future work will apply and downsize the fiber Bragg grating (FBG)-based distal force

sensor<sup>[67,68]</sup> for instrument integration and attach quasi-distributed optical fibers embedded with multiple FBG elements or the optical frequency domain reflectometry (OFDR) with fully distributed strain sensors<sup>[69]</sup> to realize both force and shape sensing to support the closed-loop control implementation.

## 5. Conclusion

A novel and practical distal continuum joint that adopts a tendon-driven helical spring-like structure and four embedded pneumatic-driven flat air tubes have been designed to achieve continuous stiffness regulation. The proposed variable stiffness approach that utilizes the embedded pneumatically driven approach and the homogeneous interaction between the inside wall of the helical structure and the inside flat air tubes, enables the uniform distribution of the internal friction force, and supports continuous variable stiffness regulation by controlling the input air pressure. The embedded pneumatic tubes can achieve high-pressure values to enhance structural stiffness with a small volume of compressed air, enabling rapid conversion between the flexible and rigid states and making them intrinsically safe for practical surgery. Characterization experiments have been performed to investigate

performances in terms of bending curvature, rigid-flexible conversion, and loading capacity. Phantom and ex vivo experiments have been performed to demonstrate its effectiveness for FE. The current work illustrates that the structural design method of embedding the pneumatical module into flexible components is an effective and practical approach to enabling the continuum robot with tunable stiffness capacity. Due to the easily implemented structure features, it also provides guidelines for extension in other continuum joints for MIS applications. Future work will take advantage of continuous stiffness regulation function and FBG-based sensing technique for advanced control and utilize the endoscopic techniques for improved integration to address the sterilization procedures.

## Acknowledgements

X.L. and D.S. contribute equally to this work. This work was supported in part by National Natural Science Foundation of China under Grant 51721003, Grant 92148201, Grant 62211530111, Grant 61973231, and Royal Society under IEC\NSFC\211360.

## Conflict of Interest

The authors declare no conflict of interest.

## Data Availability Statement

The data that support the findings of this study are available from the corresponding author upon reasonable request.

## Keywords

continuous stiffness adjustment, continuum joint, flexible endoscopic robots, flexible endoscopy, variable stiffness

Received: November 18, 2022

Revised: February 13, 2023

Published online: March 16, 2023

- [1] P. E. Dupont, B. J. Nelson, M. Goldfarb, B. Hannaford, A. Menciassi, M. K. O'Malley, N. Simaan, P. Valdastris, G. Yang, *Sci. Robot.* **2021**, 6, eabi8017.
- [2] G. Ciuti, K. Skonieczna-Zydecka, W. Marlicz, V. Iacovacci, H. Liu, D. Stoyanov, A. Arezzo, M. Chiurazzi, E. Toth, H. Thorlacius, P. Dario, A. Koulaouzidis, *J. Clin. Med.* **2020**, 9, 1648.
- [3] J. Zhu, L. Lyu, Y. Xu, H. Liang, X. Zhang, H. Ding, Z. Wu, *Adv. Intell. Syst.* **2021**, 3, 2100011.
- [4] D. A. Troncoso, J. A. Robles-Linares, M. Russo, M. A. Elbanna, S. Wild, X. Dong, A. Mohammad, J. Kell, A. D. Norton, D. Axinte, *IEEE Robot. Autom. Mag.* **2022**, <https://doi.org/10.1109/MRA.2022.3223220>.
- [5] S. Atallah, B. Martin-Perez, D. Keller, J. Burke, L. Hunter, *Br. J. Surg.* **2015**, 102, E73.
- [6] J. Burgner-Kahrs, D. C. Rucker, H. Choset, *IEEE Trans. Robot.* **2015**, 31, 1261.
- [7] M. T. Thai, P. T. Phan, T. T. Hoang, S. Wong, N. H. Lovell, T. N. Do, *Adv. Intell. Syst.* **2020**, 2, 1900138.
- [8] J. Zhao, J. Li, L. Cui, C. Shi, G. Wei, *Appl. Bionics Biomech.* **2021**, 2021, 6911202.
- [9] P. E. Dupont, N. Simaan, H. Choset, C. Rucker, *Proc. IEEE* **2022**, 110, 847.
- [10] C. Shi, X. Luo, P. Qi, T. Li, S. Song, Z. Najdovski, T. Fukuda, H. Ren, *IEEE Trans. Biomed. Eng.* **2016**, 64, 1665.
- [11] W. Marlicz, X. Ren, A. Robertson, K. Skonieczna-Zydecka, I. Loniewski, P. Dario, S. Wang, J. N. Plevris, A. Koulaouzidis, G. Ciuti, *Cancers* **2020**, 12, 2775.
- [12] N. Kurniawan, M. Keuchel, *Comput. Struct. Biotechnol.* **2017**, 15, 168.
- [13] A. Loeve, P. Breedveld, J. Dankelman, *IEEE Pulse* **2010**, 1, 26.
- [14] M. Manti, V. Cacucciolo, M. Cianchetti, *IEEE Robot. Autom. Mag.* **2016**, 23, 93.
- [15] L. Blanc, A. Delchambre, P. Lambert, *Actuators* **2017**, 6, 23.
- [16] M. Hwang, D.-S. Kwon, *IEEE/ASME Trans. Mech.* **2019**, 24, 2193.
- [17] J. Shang, K. Leibrandt, P. Giataganas, V. Vitiello, C. A. Seneci, P. Wisanuvej, J. Liu, G. Gras, J. Clark, A. Darzi, G. Yang, *IEEE Robot. Autom. Lett.* **2017**, 2, 1510.
- [18] P. Berthet-Rayne, K. Leibrandt, K. Kim, C. A. Seneci, J. Z. Shang, G. Yang, in *IEEE/RSJ Int. Conf. on Intelligent Robots and Systems (IROS)*, IEEE, Piscataway, NJ **2018**, p. 4964.
- [19] C. Li, Y. Yan, X. Xiao, X. Gu, H. Gao, X. Duan, X. Zuo, Y. Li, H. Ren, *IEEE Robot. Autom. Lett.* **2021**, 6, 5541.
- [20] Z. Li, L. Wu, H. Ren, H. Yu, *Mech. Mach. Theory.* **2017**, 107, 148.
- [21] W. Hong, L. Xie, J. Liu, Y. Sun, K. Li, H. Wang, *IEEE/ASME Trans. Mech.* **2018**, 23, 1226.
- [22] R. J. Hendrick, C. R. Mitchell, S. D. Herrell, R. J. Webster, 3rd, *Int. J. Robot. Res.* **2015**, 34, 1559.
- [23] Z. Mitros, S. H. Sadati, R. Henry, L. Da Cruz, C. Bergeles, *Annu. Rev. Control Robot. Auton. Syst.* **2022**, 5, 335.
- [24] J. Starke, E. Amanov, M. T. Chikhaoui, J. Burgner-Kahrs, in *IEEE/RSJ Int. Conf. on Intelligent Robots and Systems (IROS)*, IEEE, Piscataway, NJ **2017**, p. 6470.
- [25] K. Xu, J. Zhao, M. Fu, *IEEE/ASME Trans. Mech.* **2015**, 20, 2133.
- [26] N. Simaan, K. Xu, A. Kapoor, W. Wei, P. Kazanzides, P. Flint, R. Taylor, *Int. J. Robot. Res.* **2009**, 28, 1134.
- [27] Y. Chitalia, S. Jeong, K. K. Yamamoto, J. J. Chern, J. P. Desai, *IEEE Trans. Robot.* **2021**, 37, 520.
- [28] H. Wang, X. Wang, W. Yang, Z. Du, Z. Yan, *IEEE/ASME Trans. Mech.* **2021**, 26, 1022.
- [29] K. Oliver-Butler, J. A. Childs, A. Daniel, D. C. Rucker, *IEEE Trans. Robot.* **2022**, 38, 1186.
- [30] S. Sefati, R. Hegeman, I. Iordachita, R. H. Taylor, M. Armand, *IEEE Trans. Robot.* **2022**, 38, 1213.
- [31] Y. Song, S. Wang, X. Luo, C. Shi, *IEEE Trans. Med. Robot. Bionics* **2022**, 4, 38.
- [32] R. Zhao, Y. Yao, Y. Luo, *J. Med. Devices* **2016**, 10, 021002.
- [33] J. Lussi, M. Mattmann, S. Sevim, F. Grigis, C. De Marco, C. Chautems, S. Pane, J. Puigmarti-Luis, Q. Boehler, B. J. Nelson, *Adv. Sci.* **2021**, 8, 2101290.
- [34] C. Chautems, A. Tonazzini, Q. Boehler, S. H. Jeong, D. Floreano, B. J. Nelson, *Adv. Intell. Syst.* **2019**, 2, 1900086.
- [35] H. M. Le, P. T. Phan, L. Cao, J. J. Liu, S. J. Phee, *Ann. Biomed. Eng.* **2020**, 48, 1837.
- [36] J. Yan, P. Shi, Z. Xu, J. Zhao, *Soft Robot.* **2021**, 9, 625.
- [37] H. Jeon, Q. N. Le, S. Jeong, S. Jang, H. Jung, H. Chang, H. J. Pandya, Y. Kim, *IEEE Robot. Autom. Lett.* **2022**, 7, 6582.
- [38] Y. Kim, S. S. Cheng, J. P. Desai, *IEEE Trans. Robot.* **2018**, 34, 18.
- [39] D. Zhang, H. Yuan, Z. Cao, *IEEE/CAA J. Autom. Sin.* **2020**, 7, 745.
- [40] S. B. Behbahani, X. Tan, *Smart Mater. Struct.* **2017**, 26, 085014.
- [41] J. Liu, L. Yin, J. H. Chandler, X. Chen, P. Valdastris, S. Zuo, *Int. J. Med. Robot.* **2021**, 17, 1.
- [42] T. Sun, Y. Chen, T. Han, C. Jiao, B. Lian, Y. Song, *Robot. Comput.-Int. Manuf.* **2020**, 61, 101848.

- [43] H. Kim, J. M. You, M. Hwang, K. U. Kyung, D. S. Kwon, *Soft Robot.* **2022**, <https://doi.org/10.1089/soro.2021.0148>.
- [44] B. Zhao, L. Zeng, Z. Wu, K. Xu, *Mech. Mach. Theory* **2020**, *149*, 103746.
- [45] Y. J. Kim, S. B. Cheng, S. Kim, K. Iagnemma, *IEEE Trans. Robot.* **2014**, *30*, 382.
- [46] J. Kim, W.-Y. Choi, S. Kang, C. Kim, K.-J. Cho, *IEEE Trans. Robot.* **2019**, *35*, 1475.
- [47] A. Shiva, A. Stilli, Y. Noh, A. Faragasso, I. D. Falco, G. Gerboni, M. Cianchetti, A. Menciassi, K. Althoefer, H. A. Wurdemann, *IEEE Robot. Autom. Lett.* **2016**, *1*, 632.
- [48] Y. Piskarev, J. Shintake, V. Ramachandran, N. Baugh, M. D. Dickey, D. Floreano, *Adv. Intell. Syst.* **2020**, *2*, 2000069.
- [49] T. Ranzani, M. Cianchetti, G. Gerboni, I. D. Falco, A. Menciassi, *IEEE Trans. Robot.* **2016**, *32*, 187.
- [50] M. Brancadoro, M. Manti, F. Grani, S. Tognarelli, A. Menciassi, M. Cianchetti, *Front. Robot. AI* **2019**, *6*, 12.
- [51] Y. J. Kim, S. B. Cheng, S. Kim, K. Iagnemma, *IEEE Trans. Robot.* **2013**, *29*, 1031.
- [52] T. Miller-Jackson, Y. Sun, R. Natividad, C. H. Yeow, *Soft Robot.* **2020**, *7*, 408.
- [53] A. J. Loeve, D. H. Plettenburg, P. Breedveld, J. Dankelman, *IEEE Trans. Biomed. Eng.* **2012**, *59*, 542.
- [54] A. L. Trejos, S. Jayaraman, R. V. Patel, M. D. Naish, C. M. Schlachta, *Surg. Endosc.* **2011**, *25*, 186.
- [55] J. H. Lee, W. H. Shin, D. S. Kwon, in *Int. Conf. on Control, Automation and Systems (ICCAS)*, Gwangju, KR **2013**, p. 631.
- [56] V. D. Sars, S. Haliyo, J. Szewczyk, *Mechatronics* **2010**, *20*, 251.
- [57] B. P. Yeung, T. Gourlay, *Int. J. Surg.* **2012**, *10*, 345.
- [58] M. Hwang, D. S. Kwon, *Int. J. Med. Robot.* **2020**, *16*, e2078.
- [59] M. F. Traeger, D. B. Roppenecker, J. Coy, A. Fiolka, D. Wilhelm, A. Schneider, A. Meining, H. Feussner, T. C. Lueth, in *IEEE Int. Conf. on Robotics and Biomimetics (ROBIO)*, IEEE, Piscataway, NJ **2014**, p. 408.
- [60] C. Quaglia, G. Petroni, M. Niccolini, S. Caccavaro, P. Dario, A. Menciassi, *J. Mech. Des.* **2014**, *136*, 105001.
- [61] Olympus Corporation, Endoscope Overview 2022, <https://www.olympus.co.uk/medical/en/Products-and-solutions/Products/Echoendoscopes.html>, (accessed: January 2023).
- [62] C. Shi, X. Luo, J. Guo, Z. Najdovski, T. Fukuda, H. Ren, *IEEE J. Biomed. Health Inf.* **2017**, *22*, 806.
- [63] T. Wang, H. Ugurlu, Y. Yan, M. Li, M. Li, A.-M. Wild, E. Yildiz, M. Schneider, D. Sheehan, W. Hu, *Nat. Commun.* **2022**, *13*, 4465.
- [64] Y. Fu, H. Liu, W. Huang, S. Wang, Z. Liang, *Int. J. Med. Robot. Comput. Assisted Surg.* **2009**, *5*, 381.
- [65] K. Ikuta, H. Ichikawa, K. Suzuki, D. Yajima, presented at *Proc. 2006 IEEE Inter. Conf. on Robotics and Automation, 2006. ICRA 2006*, IEEE, Piscataway, NJ **2006**.
- [66] Y. Kim, E. Genevriere, P. Harker, J. Choe, M. Balicki, R. W. Regenhardt, J. E. Vranic, A. A. Dmytriw, A. B. Patel, X. Zhao, *Sci. Robot.* **2022**, *7*, eabg9907.
- [67] Z. Tang, S. Wang, M. Li, C. Shi, *IEEE Trans. Med. Robot. Bionics* **2022**, *4*, 145.
- [68] K. Sun, M. Li, S. Wang, G. Zhang, H. Liu, C. Shi, *IEEE Sens. J.* **2021**, *21*, 16681.
- [69] C. Shi, S. Giannarou, S.-L. Lee, G.-Z. Yang, presented at *2014 IEEE/RSJ Int. Conf. on Intelligent Robots and Systems*, IEEE, Piscataway, NJ **2014**.